LES of the non-isothermal transitional flow in rotating cavity

E. Tuliszka-Sznitko *, A. Zielinski, W. Majchrowski

Institute of Thermal Engineering, Poznan University of Technology, ul. Piotrowo 3, 60-965 Poznan, Poland

ARTICLE INFO

ABSTRACT

The paper presents the 3D LES study of the non-isothermal transitional and turbulent flow in rotor/stator sealed cavity with a rotating inner and a stationary outer cylinder. The stator and the outer cylinder are warmer than the rotor and the inner cylinder. Computations have been performed for the cavity of aspect ratio $L = (R_1 - R_0)/2h = 5$, curvature parameter $Rm = (R_1 + R_0)/(R_1 - R_0) = 3$, Reynolds numbers $Re = \Omega R_1^2/\nu = 75{,}000 - 300{,}000$, thermal Rossby numbers $B = \beta(T_2 - T_1) = 0.01 - 0.4$, and for the cavity ($L = 9$, $Rm = 1.5$, $Re = 100{,}000 - 150{,}000$, $B = 0.01 - 0.4$). Computations we based on the efficient pseudo-spectral Chebyshev–Fourier method (Serre, E., Pulicani, J.P., 2001. A three-dimensional pseudospectral method for rotating flows in a cylinder. Computers and Fluids, 30, 491). In Large Eddy Simulations we used a version of the dynamic Smagorinsky eddy viscosity model proposed by Meneveau (Meneveau, C., Lund, T.S., Cabot, W.H., 1996, A Lagrangian dynamic subgrid-scale model of turbulence. Journal of Fluid Mechanics, 319, 353–385), in which the averaging is performed over the particle pathline. This approach allowed us to perform computations for higher Reynolds numbers for confined rotating flows, which are strongly inhomogeneous and anisotropic. Results showed that the turbulence is concentrated mostly in the stator boundary layer with a maximum at the junction between the stator and the outer cylinder. For the cavity of aspect ratio $L = 5$ the stator boundary layer was fully turbulent for $Re \geqslant 100{,}000$, whereas the rotor boundary layer was still laminar. The influence of the thermal Rossby number on the flow structure and the basic state was not significant. The correlation formulas, for predicting the distribution of local Nusselt numbers along disks as well as the correlation formulas for the averaged Nusselt numbers depending on the Reynolds numbers are given on the basis of our results.

© 2009 Elsevier Inc. All rights reserved.

1. Introduction

This study concerns the numerical prediction of the transitional and turbulent flows with heat transfer in an enclosed rotor/stator cavity. The problem is not only very interesting from the point of view of fundamental fluid mechanics but it is also a topic of practical importance. The flow in the rotating cavity is of great interest for the internal aerodynamics of engines, especially for the optimization of turbomachinery air-cooling devices. The experimental investigations in the rotating cavities are very difficult and expensive. In this situation, numerical simulations, particularly Direct Numerical Simulation (DNS) and Large Eddy Simulation (LES), which can deliver precise knowledge on the flow structure in the rotating cavity become indispensable tools.

One of the first experimental investigations of the flow in sealed rotor/stator configurations was performed by Daily and Nece (1960). Daily and Nece (1960) found that the flow structure depends on the Reynolds number $Re = \Omega R_1^2/\nu$ and the aspect ratio $L = (R_1 - R_0)/2h$. They divided flows in rotating cavities into four regimes depending on the combination of the Reynolds number Re

and aspect ratio L: two laminar (I and II) and two turbulent (III and IV) regimes. Regimes I and III correspond to flows with merged boundary layers and regimes II and IV to flows with separated boundary layers. Heat transfer at a single rotating disk was investigated by Goldstein (1935), Cobb and Saunders (1956) and Dorfman (1963). Nikitenko (1963) performed experimental investigation of the flow in the enclosed rotor/stator cavity, where both disks were isothermal, for the aspect ratio in a wide range $11.8 < L < 55.5$ and for $Re < 10^6$. Nikitenko (1963) did not notice effect of the aspect ratio L on the local Nusselt number distribution. He correlated his results for laminar and turbulent flows as follows: $Nu_r = r\,\alpha/\lambda = 0.675 Re_r^{0.5}$, $Nu_r = 0.0217 Re_r^{0.8}$ (α is the heat transfer coefficient, λ is the thermal conductivity of the fluid, Re_r is the local Reynolds number). Owen et al. (1974) investigated experimentally the flow in the cavity with throughflow; cooling air was introduced through a hole in the centre of an adiabatic stator, and a parabolic profile of temperature was kept on the rotor. Owen et al. (1974) showed that for the aspect ratio in the range $55.5 < L < 166.6$ the averaged Nusselt number increases with increasing L (Owen found that for smaller L the Nusselt number is independent from L). Schukin and Olimpiev (1975) measured the averaged Nusselt numbers in a rotating cavity of aspect ratio $L = 15.5$. The radial distribution of temperature on the rotor varied

* Corresponding author. Tel.: +48 61 6652111; fax: +48 61 665 2281.
E-mail address: ewa.tuliszka-sznitko@put.poznan.pl (E. Tuliszka-Sznitko).

Notations

a	thermal diffusivity (m^2/s)
B	thermal Rossby number ($=\beta(T_2 - T_1)$)
C_S	Smagorinsky coefficient
h	half of the distance between disks (m)
H	ramp function
L	aspect ratio ($=(R_1 - R_0)/2h$)
N, K, M	number of collocation points in radial, azimuthal and axial directions
Nu_r	local Nusselt number ($=\alpha r/\lambda$)
Nu_{avg}	averaged Nusselt number
p^*	dimensionless pressure
P	pressure (N/m^2)
Pr	Prandtl number ($=0.71$)
Pr_{SGS}	SGS Prandtl number
r^*, ϕ, z^*	dimensionless cylindrical coordinates
r, ϕ, z	dimension cylindrical coordinates (m), (rad), (m)
$\bar{r}$	dimensionless radial coordinate ($=r/h$)
Rm	curvature parameter ($=(R_1 + R_0)/(R_1 - R_0)$)
R_0	radius of the inner cylinder (m)
R_1	radius of the outer cylinder (m)
Re	Reynolds number ($= \Omega R_1^2/v$)
Re_r	local Reynolds number ($=\Omega r^2/v$)
S_{ij}	rate of strain tensor
t	time (s)
t^*	dimensionless time
T	temperature (K)
T_1, T_2	temperature of rotor and stator (K)
T_n, T_m	Chebyshev polynomials
V	velocity vector (m/s)

u^*, v^*, w^*	dimensionless velocity components in radial, azimuthal and axial direction
x^*	dimensionless position along the particle pathline in considered time $n + 1$

Greek symbols

α	coefficient of heat transfer (W/m^2 K)
α_j^{SGS}	subgrid-scale energy flux
δ	thickness of the boundary layer (m)
β	thermal expansion coefficient, $1/(K)$
Δ	filtering width
ε	weighting function
λ	coefficient of thermal conductivity (W/m K)
μ	dynamic viscosity (kg/s m)
v	kinetic viscosity (m^2/s)
v_{SGS}	subgrid-scale eddy viscosity
ρ	density (kg/m^3)
T^*	dimensionless temperature ($=(T - T_1)/(T_2 - T_1)$)
σ_{ij}^{SGS}	subgrid-scale stress tensor
τ	time scale
Ω	rotation of the rotor (rad/s)

Subscripts and superscripts

c	inviscid core
$n, n + 1$	time sections
w	parameters at the wall
–	filtering at scale Δ
Λ	filtering at scale 2Δ
1 and 2	indicate rotor and stator

with r^n ($0 < n < 0.6$). Measurements were performed in the transitional ($10^5 < Re < 10^6$) and turbulent regimes ($10^6 < Re < 3 \times 10^8$). For a temperature profile with $n = 0.25$ and for turbulent flow, Schukin and Olimpiev (1975) proposed the correlation $Nu_{avg} = 0.0168Re^{0.8}$. All earlier theoretical and numerical works were summarized by Owen and Rogers (1989, 1995). Itoh et al. (1990) performed measurements of the mean velocity and of the Reynolds stress tensor components for a wide range of parameters in an enclosed cavity of the aspect ratio 12.5. Djaoui and Debuchy (1998) measured the Reynolds stresses in the rotor/stator cavity of a large aspect ratio with throughflow, using the hot and cold wire anemometry technique. Pellé and Harmand (2007) performed measurements over the rotor (in the open rotor/stator configuration), using a technique based on infrared thermography. They determined the distribution of the local convection heat transfer coefficient on the rotor and analyzed the influence of the Reynolds number Re and the aspect ratio L on α.

Numerical modeling of the flow in the rotor/stator cavity turned out to be a difficult problem mostly due to the fact that in the cavity simultaneously exist areas of laminar, transitional and turbulent flow which are completely different in terms of flow properties. The first numerical modeling in the rotor/stator cavity was performed by Morse (1987) who used a modified version of the low Reynolds number k–ε model proposed by Launder and Sharma (1974). Chew and Vaughan (1988) solved the Reynolds equations in the rotor/stator cavity using a finite difference method and a mixing length model. They received a good agreement with Daily and Nece (1960) experimental data. Some advanced heat transfer models were developed by Nagano et al. (1991), Iacovides and Toumpanakis (1993), Elena and Schiestel (1995, 1996), Abe et al. (1996), Poncet and Schiestel (2007). Poncet and Schiestel (2007) performed detailed computations using an RSM model for

the rotor/stator cavity with axial inflow and outflow ($L = 2.25$, 12.5 and 27.7).

At the beginning of the present decade, numerical methods like DNS, and for fully turbulent flow-LES, became a valuable tool in predicting the flow structures and heat transfer effect. Most of studies using DNS were dedicated to instability of the flow in shrouded cavities (Serre and Pulicani, 2001; Serre et al., 2001, 2004a,b; Healey, 2007; Craspo del Arco et al., 1996; Moisy et al., 2004; Jacques et al., 2002; Randriamampianina and Poncet, 2006; Lopez et al., 2002; Tuliszka-Sznitko et al., 2002, 2007, 2009; Tuliszka-Sznitko and Zielinski, 2008; Czarny et al., 2002). The main contribution concerning turbulent flow (using DNS) came from Lygren and Andersson (2001) who provided a detailed description of coherent structures in the near-disk areas. The first LES computations of the flow around a single rotating disk were performed by Wu and Squires (2000). Lygren and Andersson (2004), Andersson and Lygren (2006) and then Séverac et al. (2007) and Séverac and Serre (2007) performed LES numerical computations for a sealed cavity. Séverac et al. (2007) used Spectral Vanishing Viscosity (SVV) method and compared the results with their LDV exper-
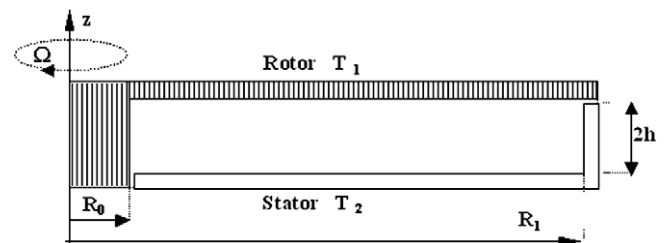

Fig. 1. Schematic picture of the rotating cavity.

imental data. SVV technique, developed among others by Pasquetti (2006), turned out to be very effective numerical tool for investigation of the turbulent flow in the rotating cavities.

DNS and LES for the non-isothermal flow in rotating cavities are not numerous (Randriamampianina et al., 1987; Serre et al., 2004a; Tuliszka-Sznitko et al., 2007, 2009; Tuliszka-Sznitko and Zielinski, 2008; Poncet and Serre, 2008).

This paper is devoted to a study of the turbulent and transitional flow with heat transfer in sealed rotor/stator cavities of aspect ratios 5 and 9. The cavity is heated from below and from the outer end-wall, whereas the rotor and the inner cylinder are cooled (Fig. 1). The main motivation of our work is to analyze the properties of turbulence of the non-isothermal flow dominated by Coriolis and centrifugal forces. In Section 2 the geometrical and mathematical models are given and the numerical approach is described. Section 3 is devoted to the mean flow and temperature field obtained for the cavity of aspect ratio $L = 5$ and 9. In Section 4 turbulent fields are discussed. The distributions of the local Nusselt number along the rotor and stator for different thermal conditions are presented in Section 5. Conclusions and closing remarks are given in Section 6.

2. Numerical modeling

2.1. Geometrical model

The geometrical domain is presented in Fig. 1. The upper disk rotates at a uniform angular velocity Ω around the central axis. The outer cylinder of radius R_1 and inner cylinder of radius R_0 are attached to the stator and rotor, respectively. The interdisk spacing is denoted by $2h$. The flow is controlled by the following physical parameters: the Reynolds number, based on the external radius of the disks R_1 and on the angular velocity of the rotor, $\mathrm{Re} = \Omega R_1^2/\nu$, the local Reynolds number $\mathrm{Re}_r = r^2\Omega/\nu$, the aspect ratio $L = (R_1 - R_0)/2h$, the curvature parameter $\mathrm{Rm} = (R_1 + R_0)/(R_1 - R_0)$, the Prandtl number $\mathrm{Pr} = 0.71$ and the thermal Rossby number $B = \beta(T_2 - T_1)$ (where β is the thermal expansion coefficient, T_1 is the temperature of the upper rotating disk and the inner cylinder, and T_2 indicates the temperature of the stator and the outer cylinder).

2.2. Numerical approach

The flow is described by the continuity, Navier–Stokes and energy equations. The equations are written in a cylindrical coordinate system (r, ϕ, z), with respect to a rotating frame of reference:

$$\nabla \cdot \mathbf{V} = 0 \tag{1a}$$

$$\rho \frac{\partial \mathbf{V}}{\partial t} + \rho(\mathbf{V} \cdot \nabla)\mathbf{V} + \rho\Omega \times (\Omega \times r) + 2\rho\Omega \times \mathbf{V} = -\nabla P + \mu\Delta\mathbf{V} \tag{1b}$$

$$\frac{\partial T}{\partial t} + (\mathbf{V} \cdot \nabla)T = a\Delta T \tag{1c}$$

where t is time, r is radius, P is pressure, ρ is density, V is the velocity vector, a is the thermal diffusivity and μ is the dynamic viscosity.

To take into account the buoyancy effects induced by the involved body forces i.e. the Coriolis force and the circumferential force (the gravity force is neglected, for its magnitude is small compared to the centrifugal force), the Boussinesq approximation is used.

$$\rho = \rho_r[1 - \beta(T - T_1)] \tag{1d}$$

where $\beta = -1/\rho_r(\partial\rho/\partial T)_p$. However, for validity of the Boussinesq approximation, the values of B have been limited to $B \leqslant 0.4$ in this study. The Prandtl number, the specific heat at constant pressure and the dynamic viscosity are constant in the present simulation. The time, length and velocity are normalized as follows: $(\Omega)^{-1}$, h and ΩR_1. The dimensionless axial coordinate is $z^* = z/h$; $z^* \in [-1, 1]$. The radius coordinate $\bar{r} = r/h$ is additionally normalized to obtain the domain $[-1, 1]$, required by the spectral method based on the Chebyshev polynomials: $r^* = (2r - (R_1 + R_0))/(R_1 - R_0)$. The dimensionless temperature is defined in the following manner: $T^* = (T - T_1)/(T_2 - T_1)$. The dimensionless components of the velocity vector in radial, azimuthal and axial directions are denoted by u^*, v^*, w^* and dimensionless pressure is denoted by p^*. The no slip boundary conditions are applied to all rigid walls, so $u^* = w^* = 0$. For the azimuthal velocity component, the boundary conditions are $v^* = 0$ on the top rotating disk, and $v^* = -(\mathrm{Rm} + r^*)/(\mathrm{Rm} + 1)$ on the stator. However, in order to eliminate the singularity of the azimuthal velocity component at the junction between the stationary outer end-wall and the rotating disk, and between the rotating inner cylinder and stator, the azimuthal velocity component was regularized by using exponential azimuthal velocity profiles:

$$v^* = -1 + e^{(z^*-1)/0.004} \tag{2a}$$

$$v^* = -\frac{\mathrm{Rm} - 1}{\mathrm{Rm} + 1}e^{(-z^*-1)/0.004} \tag{2b}$$

These profiles provide reasonable representation of experimental conditions at the radial and axial gaps (Fig. 1). According to the paper by Tavener et al. (1991), in which the authors investigated experimentally and numerically the flow in a rotating annular cavity, if the gaps are sufficiently small, the effect of the form of function used to describe azimuthal velocity profiles on the cylinders, on the flow patterns away from the closest vicinity of singularities is negligibly small. Problem of regularization formulas are also discussed in Randriamampianina et al. (1997, 2001).

The numerical code prepared in the present research for LES of the non-isothermal flow in the annular cavity (described in details in Tuliszka-Sznitko et al., 2009) is an extended version of the DNS code developed in Prof. P. Bontoux group (Hugues and Randriamampianina, 1998; Serre and Pulicani, 2001; Raspo et al., 2002). The numerical solution is based on a pseudo-spectral Chebyshev–Fourier–Galerkin approximation; the approximation of the flow variables $\Psi = (u^*, w^*, v^*, p^*, T^*)$ is given by a development in truncated series:

$$\Psi_{NMK}(r^*, z^*, \varphi, t^*) = \sum_{p=-K/2}^{K/2-1} \sum_{n=0}^{N} \sum_{m=0}^{M} \hat{\Psi}_{nmp}(t^*)T_n(r^*)T_m(z^*)e^{ip\varphi},$$
$$-1 \leq r^*, z^* \leq 1; \quad 0 \leq \varphi \leq 2\pi \tag{3}$$

Table 1
Geometrical and physical parameters of considered flow cases. Range of the thermal Rossby number used in computations. Number of collocation points used in radial, azimuthal and axial directions (N, K, M). The dimensionless time step δt^*.

| L	Rm	Re	B	Mesh	δt^*
5	3	0.2×10^5 (DNS)	0.1	$(64 \times 95 \times 51)$	0.005
		0.75×10^5 (LES), 10^5 (LES/DNS),	0.01–0.4	$(125 \times 125 \times 81)$	0.001
		1.5×10^5(LES), 2×10^5 (LES),	0.01–0.4	$(125 \times 125 \times 81)$	0.001–0.0005
		2.5×10^5 (LES), 3×10^5 (LES)	0.1	$(150 \times 150 \times 81)$	0.0005
9	1.5	0.75×10^5(LES), 10^5(LES),	0.01–0.4	$(125 \times 125 \times 81)$	0.001
		1.25×10^5 (LES), 1.5×10^5(LES)	0.01–0.4	$(150 \times 150 \times 81)$	0.001–0.0005
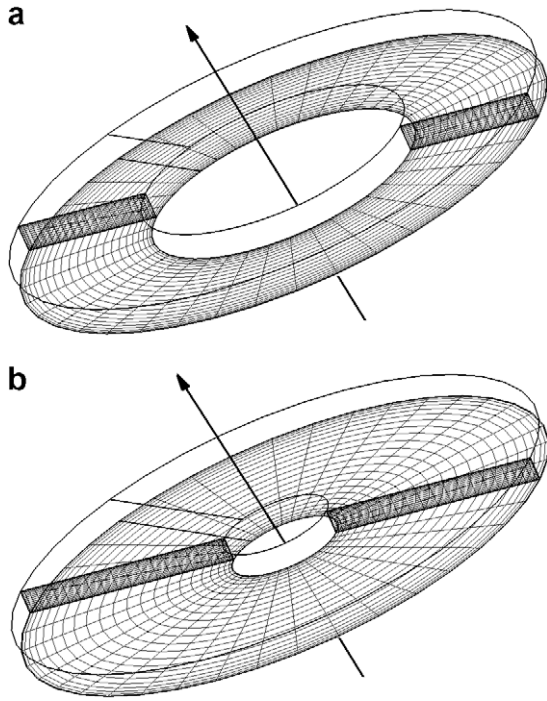
Fig. 2. The 3D views of geometrical annular cavities: (a) ($L = 5$, Rm = 3) and (b) ($L = 9$, Rm = 1.5).

where $T_n(r)$ and $T_m(z)$ are Chebyshev polynomials of degrees n and m, respectively, t^* is dimensionless time, and N, K and M are the numbers of collocation points in the radial, azimuthal and axial directions, respectively. The Gauss–Lobatto collocation points in radial and axial directions are used: $r_i^* = \cos(\pi i/N)$ for $0 \leqslant i \leqslant N$ and $z_i^* = \cos(\pi i/M)$ for $0 \leqslant i \leqslant M$ to ensure high accuracy of the solution inside the very narrow boundary layers at the disks. The uniform mesh has been used in the azimuthal direction; $\phi_k = 2\pi k/K$, $k = 0$, 1, 2...$K - 1$. The number of collocation points (N,K,M) used in computations depends on analyzed flow cases; detailed information are included in Table 1. The initial condition corresponds to the fluid at rest. The time scheme is semi-implicit and second-order accurate; it corresponds to a combination of the second-order backward differentiation formula for viscous diffusion terms and the Adams–Bashforth scheme for non-linear terms. The dimensionless time step is $\delta t^* = 0.001$–0.0005. The method uses a projection scheme to maintain the incompressibility constraint.

In the LES, after a filtering operation has been applied to the governing equations, with filter width equal to the grid spacing in azimuthal direction, we obtained the filtered equations of motion (Tuliszka-Sznitko et al., 2009). Subgrid-scale stress tensor σ_{ij}^{SGS} and energy flux α_j^{SGS} are expressed as:

$$\sigma_{ij}^{SGS} = -2\nu_{SGS}\bar{S}_{ij} \tag{4a}$$

$$\alpha_j^{SGS} = \frac{\nu_{SGS}}{Pr_{SGS}} \frac{\partial \zeta^{*k}}{\partial x_j^*} \frac{\partial \bar{T}^*}{\partial \zeta^{*k}} \tag{4b}$$
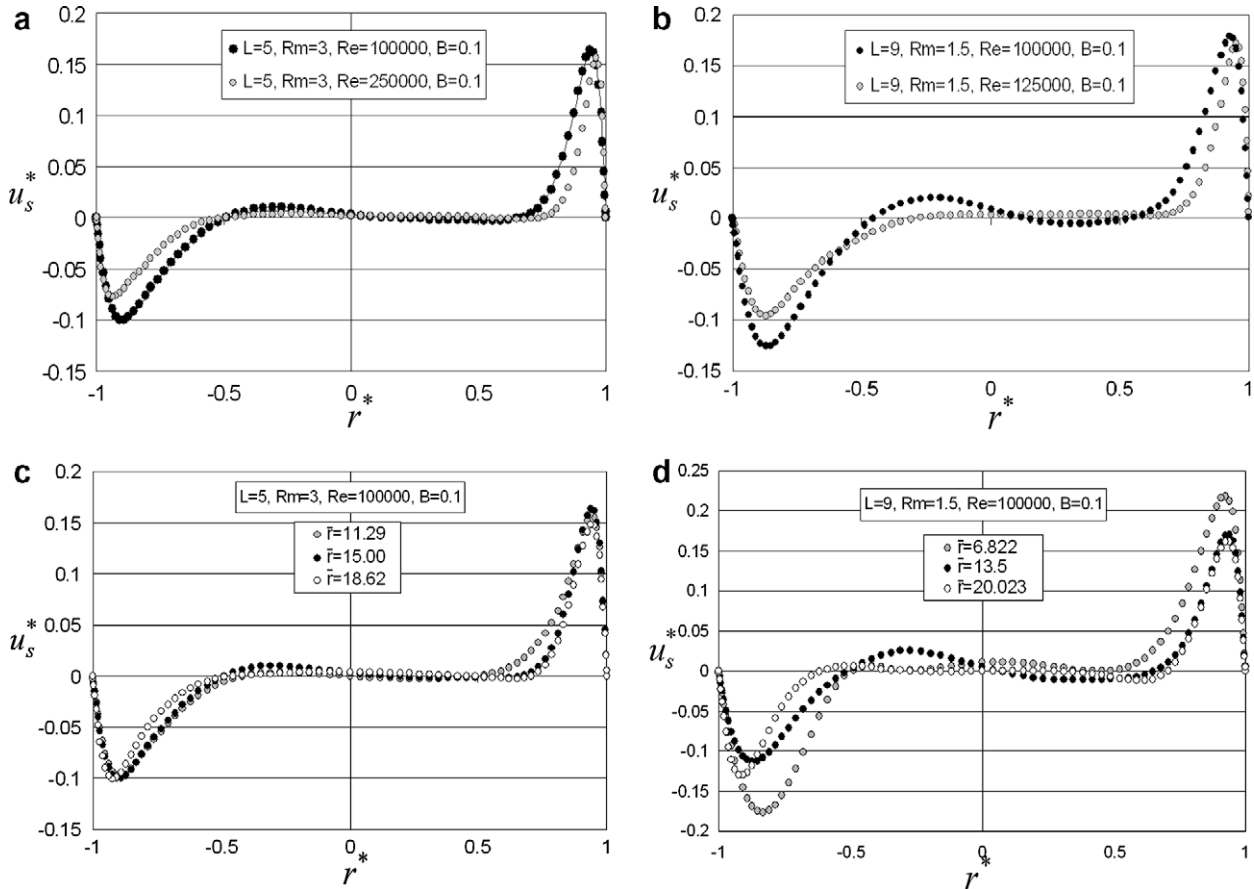
Fig. 3. Axial profiles of the radial velocity component obtained from LES for (a) ($L = 5$, Rm = 3, $B = 0.1$) and for different Re, (b) ($L = 9$, Rm = 1.5, $B = 0.1$) and for different Re, (c) ($L = 5$, Rm = 3, Re = 100,000, $B = 0.1$) and for different sections of the cavity, (d) ($L = 9$, Rm = 1.5, Re = 100,000, $B = 0.1$) and for different sections of the cavity.

$$\bar{S}_{ij} = \frac{1}{2}\left(\frac{\partial \zeta^{*k}}{\partial x_j^*}\frac{\partial \bar{u}_i^*}{\partial \zeta^{*k}} + \frac{\partial \zeta^{*k}}{\partial x_i^*}\frac{\partial \bar{u}_k^*}{\partial \zeta^{*k}}\right) \tag{5a}$$

$$v_{SGS} = C_S^2\Delta^2\sqrt{2\bar{S}_{ij}\bar{S}_{ij}} \tag{5b}$$

where filtered dependent variables are indicated by overbars. In the above equations $(x_1^*,x_1^*,x_1^*) = (x^*,y^*,z^*)$ and $(\zeta^{*1},\zeta^{*2},\zeta^{*3}) = (r^*,\phi,z^*)$. In our computations, we used a version of the dynamic Smagorinsky eddy viscosity model (Germano et al., 1991) proposed by Meneveau et al. (1996). Meneveau et al. (1996) accumulated the required averaging over the fluid particle pathlines, instead of averaging over the direction of statistical homogeneity. In this approach the Smagorinsky coefficient, at a given position x, depends on the history of the flow along the pathline. In the present research the approach from Meneveau et al. (1996) was used to perform computations in the rotating cavity because this class of flows is statistically homogeneous only in the azimuthal direction. The Smagorinsky coefficient is determined by minimizing the modeling error over the pathline of the fluid particle:

$$C_S^2 = \frac{L_{LM}}{L_{MM}} \tag{6}$$

where

$$L_{LM}^{n+1}(x^*) = H\left(\varepsilon(L_{ij}M_{ij})^{n+1}(x^*) + (1-\varepsilon)L_{LM}^n(x^* - \bar{u}^*\Delta t^*)\right) \tag{7a}$$

$$L_{MM}^{n+1}(x^*) = \varepsilon(M_{ij}M_{ij})^{n+1}(x^*) + (1-\varepsilon)L_{MM}^n(x^* - \bar{u}^*\Delta t^*) \tag{7b}$$

In the above equations x^* is the position of particle in considered time $n+1$ and $(x^* - \bar{u}^*\Delta t^*)$ is the position of the same particle at

the previous time n, $\bar{u}^*$ is the velocity computed in time n, H is a ramp function ($H(a) = a$ if $a > 0$ and zero otherwise), ε is the weighting function (Meneveau et al. 1996):

$$\varepsilon = \frac{\Delta t^*/\tau^n}{1 + \Delta t^*/\tau^n} \tag{8}$$

where τ is the dimensionless time scale over which the averaging is performed. Meneveau et al. (1996) gives some possible choices for τ based on the requirement, that the model should be purely dissipative, ensuring numerical stability. In this paper we used the following function for the time scale τ:

$$\tau = 1.5\Delta(M_{ij}M_{ij})^{-1/4} \tag{9}$$

where

$$M_{ij} = 2\Delta^2\left[|\widehat{\bar{S}|\bar{S}_{ij}} - 4|\widetilde{\bar{S}}|\widetilde{\bar{S}}_{ij}\right] \tag{10a}$$

$$L_{ij} = \widehat{\bar{u}_i\bar{u}_j} - \tilde{\bar{u}}_i\tilde{\bar{u}}_j \tag{10b}$$

In the above equations $\overline{(\cdot)}$ represents filtering with scale Δ and $\widehat{(\cdot)}$ represents filtering with scale 2Δ. For the non-isothermal flow we adopted Lilly's approach to the Lagrangean model (Lilly 1992). We introduced the turbulent Prandtl number denoted by Pr_{SGS} (Tuliszka-Sznitko and Zielinski, 2008; Tuliszka-Sznitko et al., 2009):

$$\frac{1}{Pr_{SGS}} = \frac{L_{PRMM}^{n+1}}{L_{RRML}^{n+1}} \tag{11}$$

where
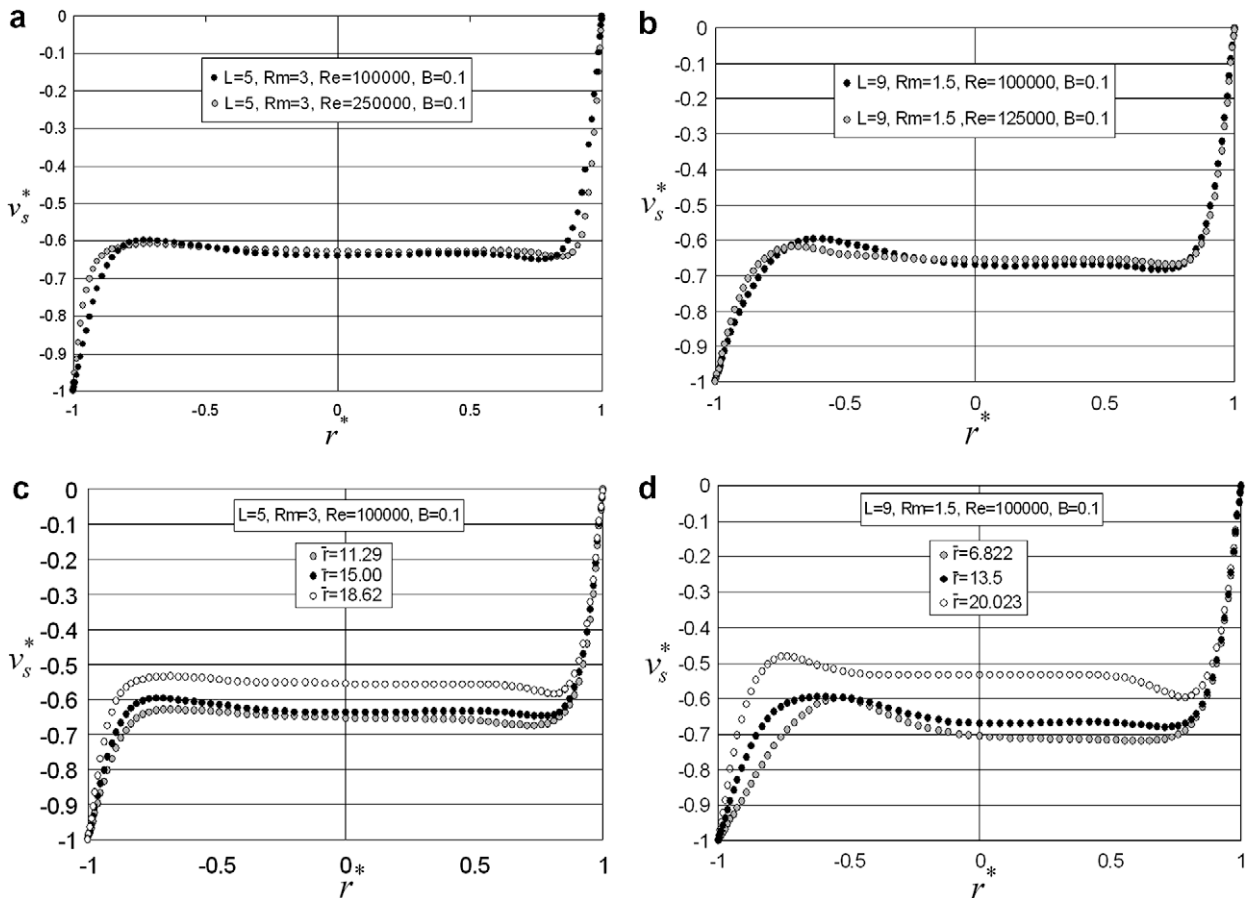
Fig. 4. Axial profiles of the azimuthal velocity component obtained from LES for (a) ($L = 5$, Rm = 3, $B = 0.1$) and for different Re, (b) ($L = 9$, Rm = 1.5, $B = 0.1$) and for different Re, (c) ($L = 5$, Rm = 3, Re = 100,000, $B = 0.1$) and for different sections of the cavity, (d) ($L = 9$, Rm = 1.5, Re = 100,000, $B = 0.1$) and for different sections of the cavity.

a

b
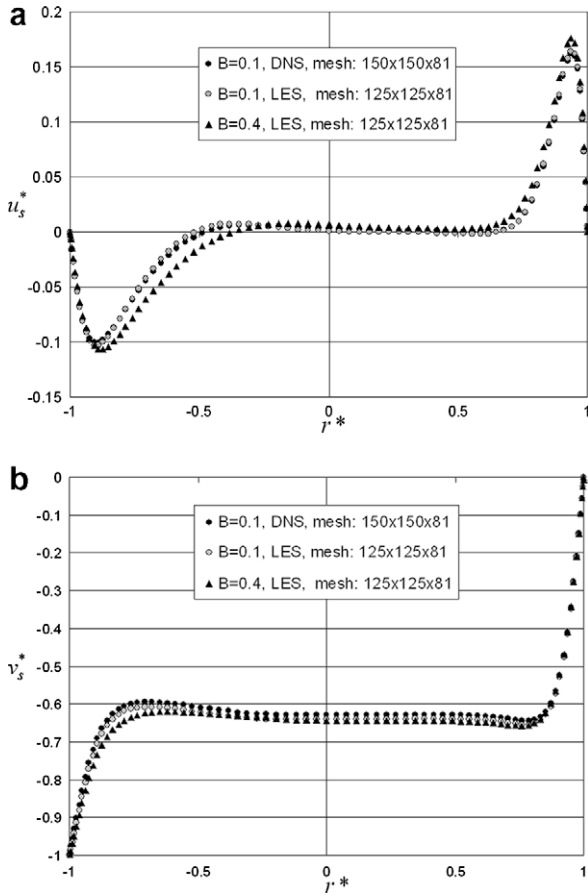
Fig. 5. Axial profiles of (a) the radial, (b) azimuthal velocity components obtained for ($L = 5$, Rm = 3, Re = 100,000, $B = 0.1$, 0.4) by LES ($125 \times 125 \times 81$) and by DNS ($150 \times 150 \times 81$) in the middle section of the cavity.
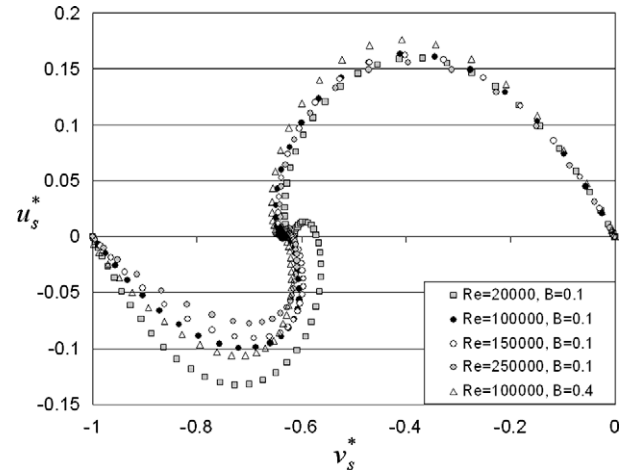
Fig. 6. Polar plots of the radial and azimuthal velocity components of velocity obtained for different Re in the middle section of the cavity ($L = 5$, Rm = 3, $B = 0.1$, 0.4).
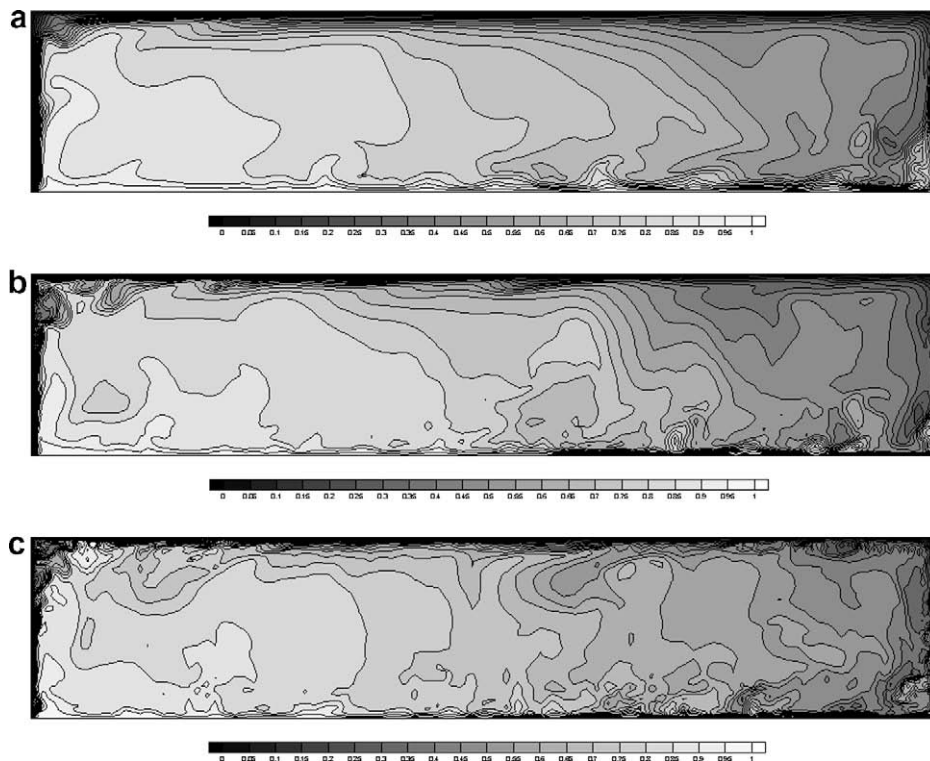
$$L_{\mathrm{PRMM}}^{n+1}(x^*) = H\Big(\varepsilon \big(P_j R_j M_{ij} M_{ij}\big)^{n+1}(x^*) + (1 - \varepsilon)L_{\mathrm{PRMM}}^n(x^* - \bar{u}^* \Delta t^*) \Big)$$

(12a)

$$L_{\mathrm{RRML}}^{n+1}(x^*) = \varepsilon \big(R_j R_j M_{ij} L_{ij}\big)^{n+1}(x^*) + (1 - \varepsilon)L_{\mathrm{RRML}}^n(x^* - \bar{u}^* \Delta t^*)$$

(12b)
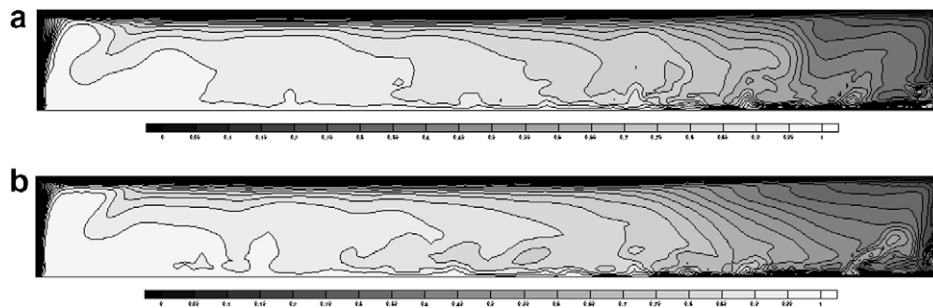
3. Mean flow

3.1. Flow field

Computations were performed for two geometrical annular cavities, ($L = 5$, Rm = 3) and ($L = 9$, Rm = 1.5) whose 3D views are

a

b

c

Fig. 7. The iso-lines of the dimensionless temperature T^* obtained for (a) Re = 100,000, (b) Re = 200,000, and (c) Re = 300,000 in the meridian section of the cavity ($L = 5$, Rm = 3.0, $B = 0.1$).

Fig. 8. The iso-lines of the dimensionless temperature T^* obtained for (a) Re = 100,000 and (b) Re = 150,000 in the meridian section of the cavity (L = 9, Rm = 1.5, B = 0.1).

shown in Fig. 2a and b, respectively. The mean and turbulent quantities computed in the frame of this research were obtained for the parameters presented in Table 1. Turbulent quantities were averaged over the dimensionless time t^* = 7–10.

The considered flows are of Batchelor type; it means that flows consist of two separated boundary layers and an inviscid core. Depending on the Reynolds number these flows can be laminar or turbulent and belong to the regime II (laminar Batchelor flow) or regime IV (turbulent Batchelor flow), respectively, according to Daily and Nece (1960) classification. Figs. 3a–d and 4a–d show the axial profiles of the radial and azimuthal velocity components, respectively. The profiles are obtained for different Re and for B = 0.1. In Figs. 3 and 4 the velocity components are normalized by $r\Omega$: $u_s^* = u^*L(Rm + 1)/\bar{r}$, $v_s^* = v^*L(Rm + 1)/\bar{r}$.

In Fig. 3a and b radial velocity component profiles obtained for different Re (B = 0.1) in the middle section (r^* = 0) of cavities (L = 5, Rm = 3) and (L = 9, Rm = 1.5) are analyzed, respectively, whereas in Fig. 3c and d the radial profiles obtained for Re = 100,000, B = 0.1 in three radial sections of considered cavities are shown. From Fig. 3 we can see that the flow consists of two separated boundary layers and an inviscid core where the radial velocity component is almost zero. In the core region, the axial velocity component is also close to zero and the azimuthal component is constant (Fig. 4). The flow is pumped radially outward along the rotor and recirculates along the stator. We can see from Fig. 3 that with increasing Re, the velocity profiles in the stator boundary layer become more turbulent. From Fig. 3d we can see that the stator boundary layer in the cavity of the aspect ratio L = 9 is turbulent only in the junction between the stator and the outer cylinder, whereas in case with L = 5 the whole stator boundary layer is turbulent. For both cases, L = 5 and L = 9 (Re = 100,000, B = 0.1), the rotor boundary layer is lami-

nar. The velocity profiles obtained in the present simulation for different Reynolds numbers have shown that the thickness of the stator boundary layer (δ_2) is approximately two times thicker than the rotor boundary layer (δ_1). For cavity (L = 5, Rm = 3, B = 0.1, Re = 100,000) we obtained δ_1/h = 0.3 for the rotor boundary layer and δ_2/h = 0.55 ($\delta_2/\delta_1 \sim 1.8$) for the stator boundary layer (r^* = 0), whereas for (L = 5, Rm = 1.8, B = 0.0, Re = 100,000) Séverac et al. (2007) obtained δ_1/h = 0.208 for the rotor boundary layer and δ_2/h = 0.444 ($\delta_2/\delta_1 \sim 2.1$) for the stator boundary layer (with the present paper normalization).

The axial profiles of the azimuthal velocity component are analyzed in Fig. 4. The LES results show a large flat core region where the azimuthal component is nearly constant. For different radial sections the azimuthal velocity components in the core are slightly
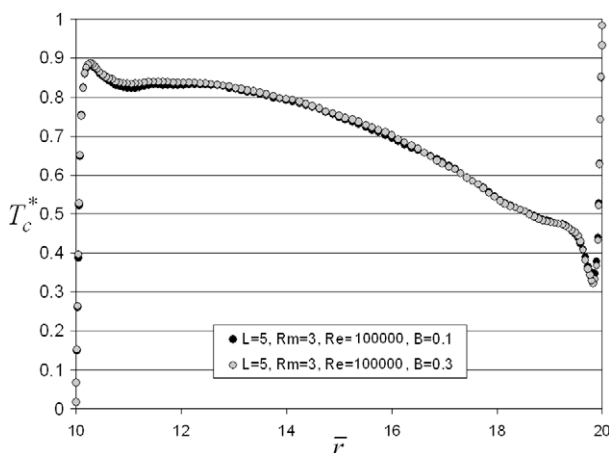
Fig. 9. The distributions of the dimensional core temperature T_c^* in terms of $\bar{r}$ obtained for (L = 5, Rm = 3, Re = 100,000, B = 0.1, 0.3).
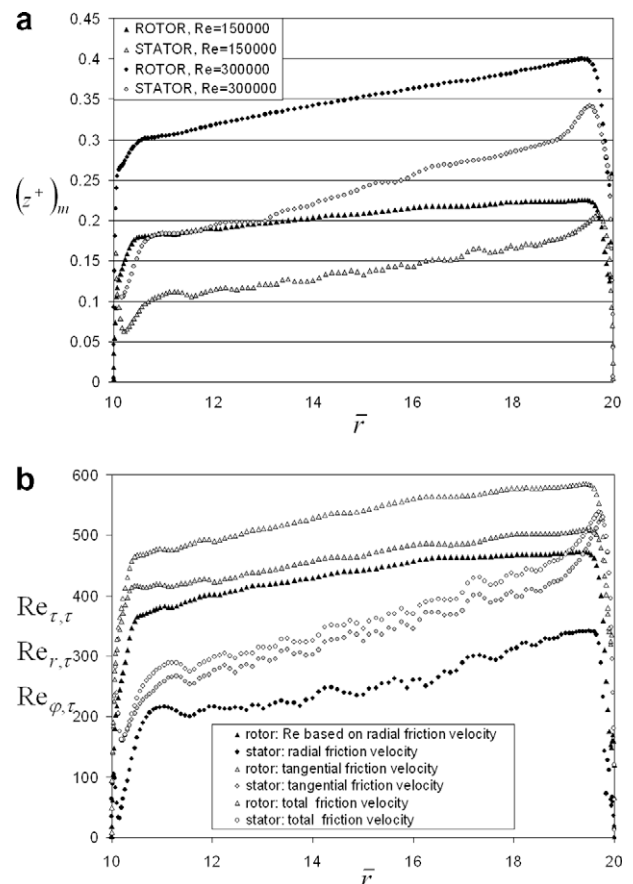
Fig. 10. (a) The distributions of $(z^+)_m$ along the rotor and stator obtained for Re = 150,000 and 300,000 (L = 5, Rm = 3, B = 0.1). (b) The Reynolds numbers based on the total (Re$_{\tau,\tau}$), radial (Re$_{r,\tau}$) and azimuthal (Re$_{\phi,\tau}$) friction velocity along the rotor and stator (L = 5, Rm = 3, Re = 150,000, B = 0.1).

different; it is probably the result of changes in the flow character along the cavity in the radial direction. From Fig. 4 we can see that the rate of rotation of the inviscid core to the rotation of rotor $K = \Omega(z^* = 0)/\Omega(z^* = 1)$ obtained from LES for ($L = 5$, Rm = 3, Re = 100,000, $B = 0.1$) in the middle section ($r^* = 0$) is $K = 0.362$, whereas for $B = 0.4$ we obtained $K = 0.357$. For ($L = 9$, Rm = 1.5, Re = 100,000, $B = 0.1$) we obtained $K = 0.33$. In the middle section of cavity ($L = 5$, Rm = 1.8, Re = 100,000, $B = 0.0$) Séverac et al. (2007) obtained 0.35 from both numerical and experimental investigations.

To verify our LES results we performed additional computations for ($L = 5$, Rm = 3, Re = 100,000, $B = 0.1$) using DNS with a more refined mesh ($150 \times 150 \times 81$). Axial profiles of the radial and azimuthal velocity components obtained by LES ($125 \times 125 \times 81$) and by DNS ($150 \times 150 \times 81$) in the middle section of the cavity are compared in Fig. 5a and b. We can see from Fig. 5a and b that the differences are small; the largest differences are observed in the central core between the azimuthal velocity components.

The positive thermal Rossby number $B > 0$ (heated stator) means that the buoyancy-driven secondary flow enforces the basic rotation driven flow. However, the influence of the thermal Rossby number on the velocity profiles is not significant. Fig. 5a and b present additionally radial and azimuthal profiles obtained by LES for $B = 0.4$.

Additional characteristics of the mean flow can be derived from polar plots of the radial and azimuthal velocity components, which describe the behavior of the 3D boundary layer. Fig. 6 shows polar plots obtained for ($L = 5$, Rm = 3, $B = 0.1$) and for different Reynolds numbers. From Fig. 6 we can see that in the near-rotor areas all LES profiles are very close to the profile obtained by DNS for a very small Reynolds number (Re = 20,000). In the stator boundary layer there are larger differences between the results obtained by LES for different Reynolds numbers; with the increasing Reynolds number, the LES polar profiles go away from the laminar solution obtained for Re = 20,000. For Re = 250,000

($L = 5$, Rm = 3) in the stator boundary layer, the form of the polar plot become more triangular, which is typical for the turbulent boundary layer (Lygren and Andersson, 2001). In the polar plot we added the profile obtained for ($L = 5$, Rm = 3, Re = 100,000, $B = 0.4$) to show the influence of the thermal Rossby number on the velocity profiles. We can see that this solution is more turbulent than solution obtained for the same Reynolds number but for $B = 0.1$.

3.2. Temperature field

Figs. 7a–c and, 8a and b show the iso-lines of the dimensionless temperature T^* obtained for Re = 100,000, 200,000 and 300,000 ($L = 5$, Rm = 3.0, $B = 0.1$) and Re = 100,000 and 1,500,000 ($L = 9$, Rm = 1.5, $B = 0.1$), respectively. We can see that for all cases the fluid is pumped along the cold rotor ($T^*(z^* = 1) = 0.0$) towards the heated outer cylinder ($T^*(r^* = 1) = 1.0$). Then the fluid is transported down and recirculates along the heated stator ($T^*(z^* = -1) = 1.0$) towards the inner cylinder. Finally, the fluid, warmed by the stator is lifted up along the cold inner cylinder ($T^*(r^* = -1) = 0.0$). The distributions of the dimensional core temperature T_c^* in terms of $\bar{r}$ obtained for ($L = 5$, Rm = 3, Re = 100,000, $B = 0.1$ and 0.3) are presented in Fig. 9. We can see that the dimensionless temperature increases very rapidly in the area near the inner cylinder from 0 at the inner cylinder up to about 0.9. Then the temperature in the core decreases gradually until the minimum value of 0.3 for the radius $\bar{r} \sim 19.8$ to reach 1 at the outer cylinder.

4. Turbulent field

To check the accuracy of mathematical description of flow near the disks, we analyzed the axial wall coordinate $(z^+)_m = z_m v_{\tau,\tau}/v$ in terms of radius $\bar{r}$, where z_m is the smallest cell in the axial direction and $v_{\tau,\tau}$ is the total friction velocity $v_{\tau,\tau} = [v^2((\partial u/\partial z)^2 + (\partial v/\partial z)^2)]^{1/4}$.
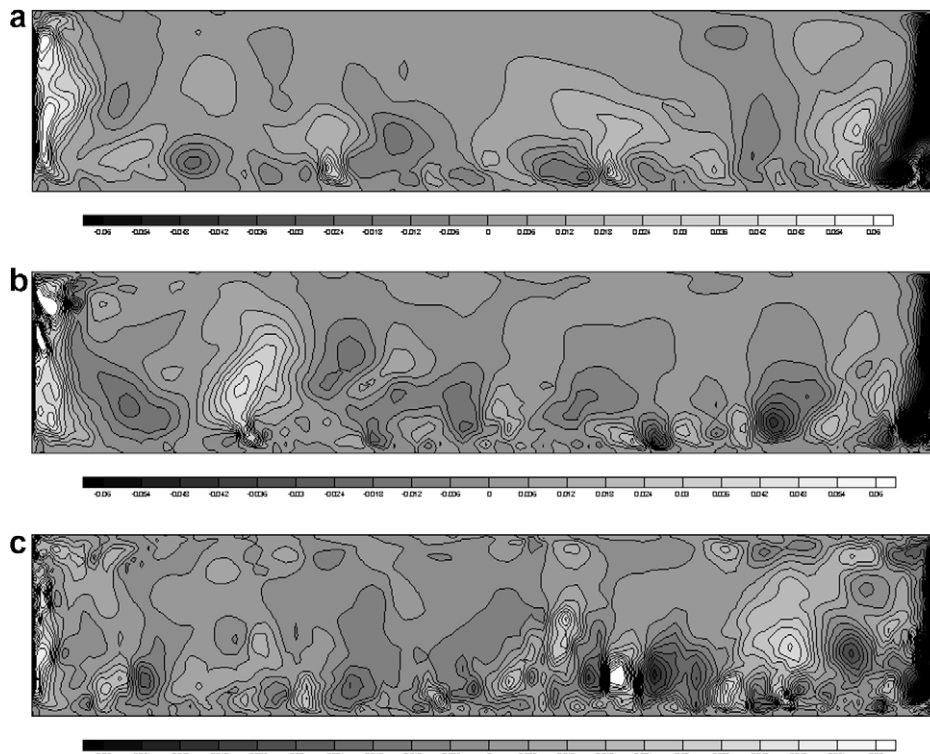

Fig. 11. The iso-lines of the axial velocity component obtained for (a) Re = 100,000, (b) 200,000, and (c) 250,000 in the meridian plane ($L = 5$, Rm = 3, $B = 0.1$)

For the mesh ($125 \times 125 \times 81$) $z_m^* = z_m/h = 0.000771$. Fig. 10a presents the distribution of $(z^+)_m$ along both disks obtained for Re = 150,000 and 300,000 ($L = 5$, Rm = 3, $B = 0.1$). We can see that $(z^+)_m$ increases gradually along both disks towards the outer cylinder reaching a maximum value $(z^+)_m = 0.4$ for Re = 300,000 (Séverac et al., 2007, used the value $(z^+)_m = 1$ as a criterion for precise description in the near-wall area). It is worthwhile to notice that $(z^+)_m$ is larger at the rotor than at the stator. In Fig. 10b the Reynolds numbers based on the total, radial and azimuthal friction velocity ($\mathrm{Re}_{\tau,\tau} = v_{\tau,\tau}(2h)/v$, $\mathrm{Re}_{r,\tau} = v_{r,\tau}(2h)/v$, $\mathrm{Re}_{\phi,\tau} = v_{\phi,\tau}(2h)/v$) are presented in terms of the dimensionless radius (Re = 150,000, $L = 5$, Rm = 3, $B = 0.1$). From Fig. 10b we can see that the Reynolds numbers $\mathrm{Re}_{\tau,\tau}$, $\mathrm{Re}_{r,\tau}$, $\mathrm{Re}_{\phi,\tau}$ increase towards the outer cylinder. The same tendency was reported by Randiamampianina et al. (2006).

To show the most disturbed regions in the meridian plane, we present the iso-lines of the axial velocity component obtained for Re = 100,000, 200,000 and 250,000 in Fig. 11a–c ($L = 5$, Rm = 3,

$B = 0.1$). From Fig. 11a we can see that for Re = 100,000 the turbulence is mostly confined in the stator boundary layer with the maximum at the junction between the stator and the outer end-wall. We also observe turbulent area on the rotating inner cylinder, where disturbances coming from the stator are transported towards the rotor. For the higher Reynolds numbers more intense turbulence is also observed in the rotor boundary layer. Fig. 12a and b show the iso-lines of the azimuthal velocity component disturbances in the azimuthal sections of the stator and rotor boundary layer, respectively ($L = 5$, Rm = 3, Re = 200,000, $B = 0.1$). We can see that only the stator boundary layer is turbulent for these parameters, with increasing intensity of turbulence towards the outer end-wall. In the rotor boundary layer we observe turbulent flow only at the junctions between the rotor and the end-walls. In the rotor boundary layer, positive spiral vortices (the crossflow type I spiral vortices) are still visible, whereas in the stator boundary layer we observe thinner and more axisymmetrical structures.

Fig. 13 shows the profiles of turbulence kinetic energy normalized by wall friction k/τ_w in the stator boundary layer, obtained in the middle section of cavity ($L = 5$, Rm = 3, $B = 0.1$, $r^* = 0$) for different Reynolds numbers, $k/\tau_w = \mathrm{Re}(\overline{u^{*'}u^{*'}} + \overline{v^{*'}v^{*'}} + \overline{w^{*'}w^{*'}})/[2L(\mathrm{Rm}+1)\sqrt{(\partial u^*/\partial z^*)_w^2 + (\partial v^*/\partial z^*)_w^2}]$. We can see that our LES profiles behave properly i.e. maximum of k/τ_w there is inside the boundary layer and with the increasing Re this maximum moves closer to the disk. A similar tendency was reported in the paper by Elena and Schiestel (1995), in which an RSM model was used. More information about the intensity of the turbulence in particular areas of the cavity can be obtained from the distributions of the Reynolds stress tensor components. Figs. 14 and 15 present the comparison between axial distributions of the normal Reynolds stress tensor components in the stator and rotor boundary layers, respectively, normalized with the wall friction $\sqrt{\overline{u'u'}}/\tau_w$, $\sqrt{\overline{v'v'}}/\tau_w$, $\sqrt{\overline{w'w'}}/\tau_w$, obtained in the middle section of cavity ($L = 5$, Rm = 3, $B = 0.1$) for different Reynolds numbers Re = 100,000, 150,000, and 250,000. From Figs. 14 and 15 we can see that the turbulence is mainly concentrated in the stator boundary layer and increases with the increasing Reynolds number. All normal Reynolds stress tensor components reach their maximum inside the boundary layer, and these maximums move closer to the disks with the increasing Re. Outside the boundary layer the values of the three components decrease to a value of one order less. We can also see from Fig. 14 that in the stator boundary layer for the Reynolds numbers from the range 100,000–250,000, $\sqrt{\overline{v'v'}}/\tau_w$ overestimates 2.15–2.5 times $\sqrt{\overline{u'u'}}/\tau_w$. For the cavity of aspect ratio ($L = 9$, Rm = 1.5) this rate is even higher. Séverac
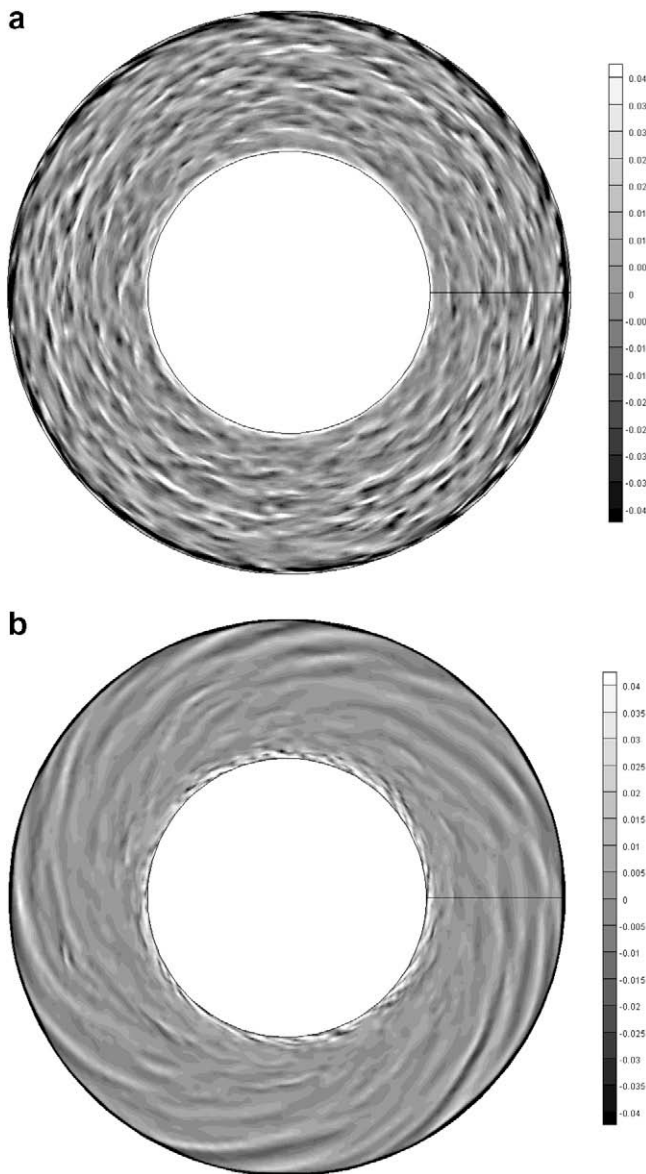

Fig. 12. The iso-lines of the azimuthal velocity component disturbances in the azimuthal sections of (a) the stator and (b) rotor boundary layer ($L = 5$, Rm = 3, Re = 200,000, $B = 0.1$).
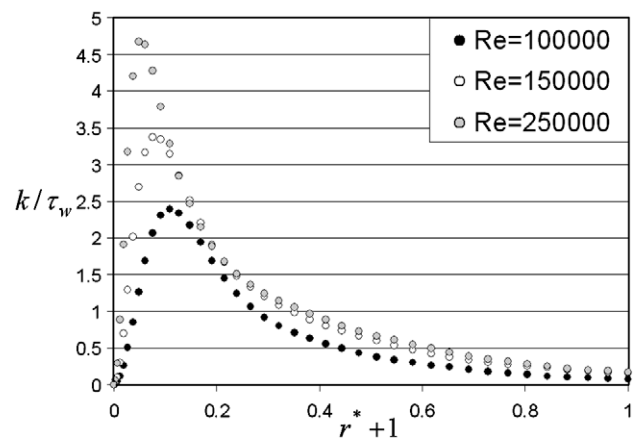

Fig. 13. The profiles of turbulence kinetic energy normalized by wall friction k/τ_w in the stator boundary layer, obtained in the middle section of cavity ($L = 5$, Rm = 3, $B = 0.1$) for different Reynolds numbers.

et al. (2007) obtained for Re = 1,000,000 (L = 5, Rm = 1.8, B = 0) overestimation equaled 2 from their SVV code but they did not observe overestimation in their experimental measurements. Itoh et al. (1990) investigated experimentally a cylindrical cavity with the aspect ratio 12 (L = 12, Rm = 1, Re = 1,000,000, B = 0) and they found that $\sqrt{\overline{v'v'}/\tau_w}$ overestimated $\sqrt{\overline{u'u'}/\tau_w}$ 1.7 times. These results show that turbulence anisotropy obtained from LES is larger than that obtained from experiments. Séverac et al. (2007) suggested that the reason for such behavior is anisotropy of the mesh, and that a more refined mesh should reduce this phenomenon. However, we compared distributions of the Reynolds stress tensor components obtained for two meshes (150 × 150 × 81) and (125 × 125 × 81) and we observed very small influence of the number of collocation points on $\sqrt{\overline{v'v'}/\tau_w}/\sqrt{\overline{u'u'}/\tau_w}$ parameter. More computations are necessary to explain this phenomenon.

Fig. 16 shows the three main Reynolds stress tensor component profiles $\overline{u^{*'}u^{*'}}, \overline{v^{*'}v^{*'}}, \overline{w^{*'}w^{*'}}$ and one shear component $\overline{u^{*'}v^{*'}}$ in terms of z^+ (shear component $\overline{u^{*'}v^{*'}}$ is the largest in comparison with $\overline{w^{*'}v^{*'}}$ and $\overline{u^{*'}w^{*'}}$) obtained for (L = 5, Rm = 3, Re = 100,000, B = 0.1) in the middle section of the cavity. From Fig. 16 we can see that in the stator boundary layer the turbulence reaches its maximum at $z^+ \sim 10$ and decreases to a value of one order less in the core (shear component $\overline{u^{*'}v^{*'}}$ is almost zero in the central core). In Randriamampianina and Poncet (2006) the maximum of $\overline{u^{*'}u^{*'}}$ was found at $z^+ \sim 8$ and the maximum of $\overline{v^{*'}v^{*'}}$ at $z^+ \sim 12$ (L = 18.32, Rm = 1.3, B = 0).

To verify our computations, we performed simulations for isothermal flow in rotor/stator cavity (L = 5, Rm = 1.8, Re = 100,000, B = 0) and we compared results with the experimental data of Séverac et al. (2007) obtained for the same geometry (Fig. 17). In

Fig. 17 the Reynolds stress component $\sqrt{\overline{u^{*'}u^{*'}}}(Rm + 1)/(Rm + r^*)$ in terms of z^* is analyzed. From Fig. 17 we can see a good agreement between the experimental data of Séverac et al. (2007) and results obtained by the present LES approach. To show influence of the thermal Rossby number on the Reynolds stress tensor component $\sqrt{\overline{u^{*'}u^{*'}}}(Rm + 1)/(Rm + r)$ in Fig. 17 the result obtained for B = 0.2 is also presented (L = 5, Rm = 1.8, Re = 100,000, B = 0.2). A detailed comparison of the results obtained by the LES approach used in the present paper and the experimental results of Séverac et al. (2007) is given in Tuliszka-Sznitko et al. (2009).

In Fig. 18 the axial distribution of averaged in time and azimuthal direction Pr_{SGS} computed from Eq. (11) is presented in function of z^* (L = 9, Rm = 1.5, Re = 150,000, B = 0.1, $r^* = 0$). We can see that the diversity of Pr_{SGS} is large.

5. Local Nusselt number distribution

One of the most important information from the engineering point of view is the distribution of the local Nusselt number in function of the radius of the disk. Most of the authors correlate the local Nusselt number by a power law such as (Pellé and Harmand 2007):

$$Nu_r = \frac{\alpha r}{\lambda} = aRe_r^b \tag{13}$$

where α is the heat transfer coefficient and λ is the thermal conductivity coefficient. Coefficient a in Eq. (13) depends on temperature boundary conditions and other characteristic parameters, whereas coefficient b changes with the nature of the flow. For laminar flow,
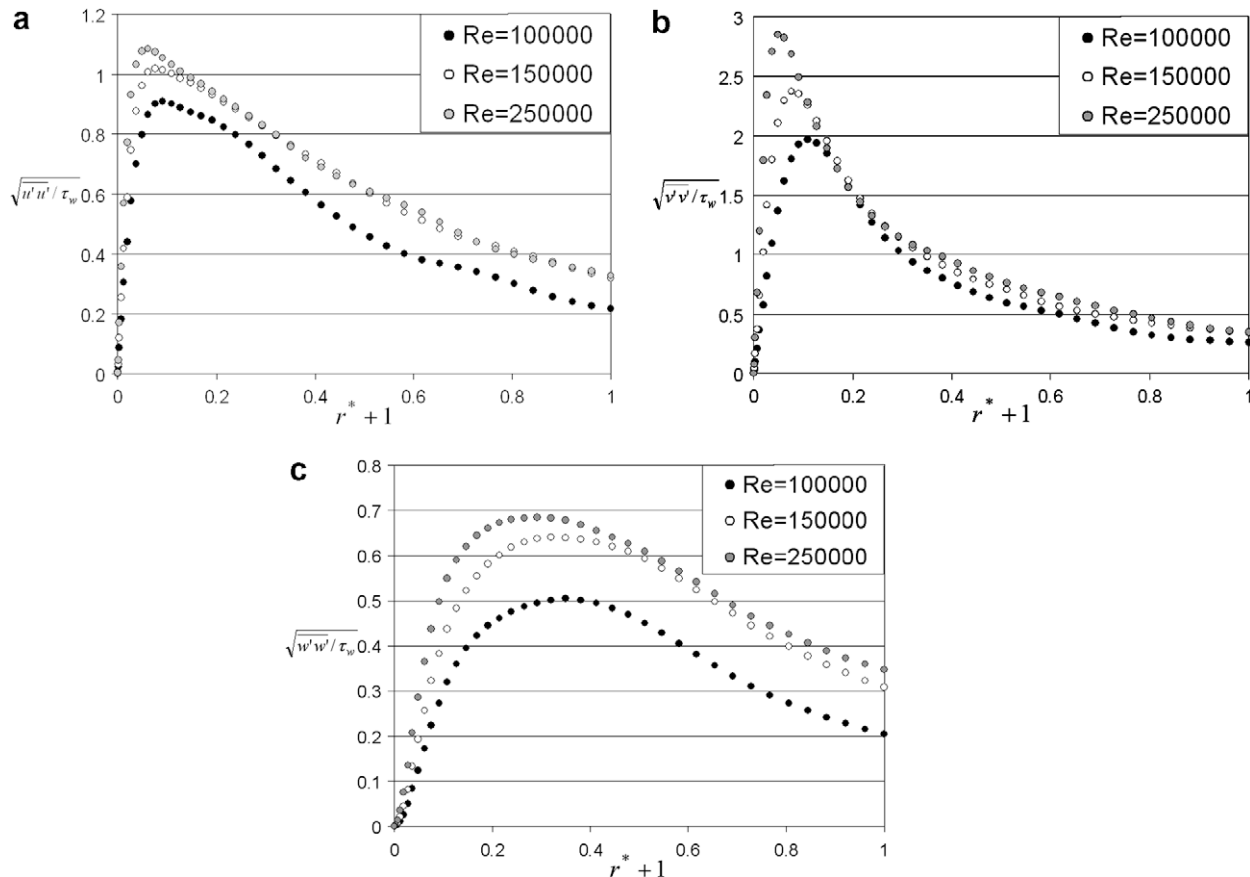

Fig. 14. The comparison between axial distributions of the normal Reynolds stress tensor components in the stator boundary layer, normalized with the wall friction. (a) $\sqrt{\overline{u'u'}/\tau_w}$, (b) $\sqrt{\overline{v'v'}/\tau_w}$, and (c) $\sqrt{\overline{w'w'}/\tau_w}$, obtained in the middle section of cavity (L = 5, Rm = 3, B = 0.1) for different Reynolds numbers.

the local convective heat transfer is independent from the radial position but increases with azimuthal speed. Consequently, the local Nusselt number varies linearly with the radius ($b = 0.5$). For turbulent flow, the local convective heat transfer coefficient increases with rotation and with radius; in most correlation formulas for turbulent flow $b \sim 0.8$. Within the frame of the present research the local Nusselt number was computed from the following equation:

$$\text{Nu}_r = \frac{\bar{r}}{T_c^*}\frac{\partial T_c^*}{\partial z^*} \qquad (14)$$

where T_c^* is the temperature of the core of cavity. Exemplary distributions of T_c^* in terms of the dimensional radius $\bar{r}$ are presented in Fig. 9. Due to the rapid changes of the core temperature T_c^* near the inner and outer cylinders these areas are excluded from Nusselt analysis.

### 5.1. Distribution of the local Nusselt numbers on the rotor

Distribution of the local Nusselt numbers along the rotor was investigated experimentally by many authors, among others by Pellé and Harmand (2007), Dorfman (1963), Nikitenko (1963), who delivered correlation functions allowing to predict the distribution of the local Nusselt numbers along disks. In most cases experimental investigations were performed for cavities with large aspect ratios, in which the confinement effect is small. Fig. 19a shows distributions of the local Nusselt numbers in terms of dimensionless radius $\bar{r}$ along the rotor, obtained in this paper for the cavity of the aspect ratio 5 ($L = 5$, $Rm = 3$, $B = 0.1$) and for different Reynolds numbers from the range Re = 75,000–250,000. We can see from Fig. 19a that the influence of the Reynolds number

on the distribution of Nusselt number is significant; with increase in Re from 75,000 to 250,000 the maximum value of Nu_r increased from 100 to 270. The distributions of the local Nusselt numbers reflect the flow structure very well. From the analysis in the previous sections we know that for all considered Re, the rotor boundary layer is laminar, however, turbulence of the rotor boundary layer increases with increasing Re. Additionally, we observe concentration of turbulence kinetic energy near cylinders, which intensifies the heat transfer in these areas. In spite of the laminar character of the flow in the rotor boundary layer ($L = 5$, $Rm = 3$), the linear part of the local Nusselt Nu_r curves observed in Fig. 19a is very short, which results from very strong confinement effect. Based on results presented in Fig. 19a we propose the following correlation function:

$$\text{Nu}_r = 0.05\text{Re}^{0.17}\text{Re}_r^{0.5} \qquad (15a)$$

The lines obtained from function (15a) are also included in Fig. 19a.

Fig. 19b shows distributions of the local Nusselt numbers in terms of dimensionless radius $\bar{r}$ along the rotor, obtained for the cavity with aspect ratio 9 ($L = 9$, $Rm = 1.5$, $B = 0.1$) and for the Reynolds numbers Re = 100,000 and 125,000. The flows in the rotor boundary layer for these parameters are purely laminar. From Fig. 19b we can see that the linear parts of the curves obtained for ($L = 9$, $Rm = 1.5$) are longer in comparison to the cases analyzed in Fig. 19a due to a smaller confinement effect (the influence of the end-walls decreases with the increasing aspect ratio of the cavity). Fig. 19b also includes the lines obtained from correlation function (15a). Results obtained from (15a) are
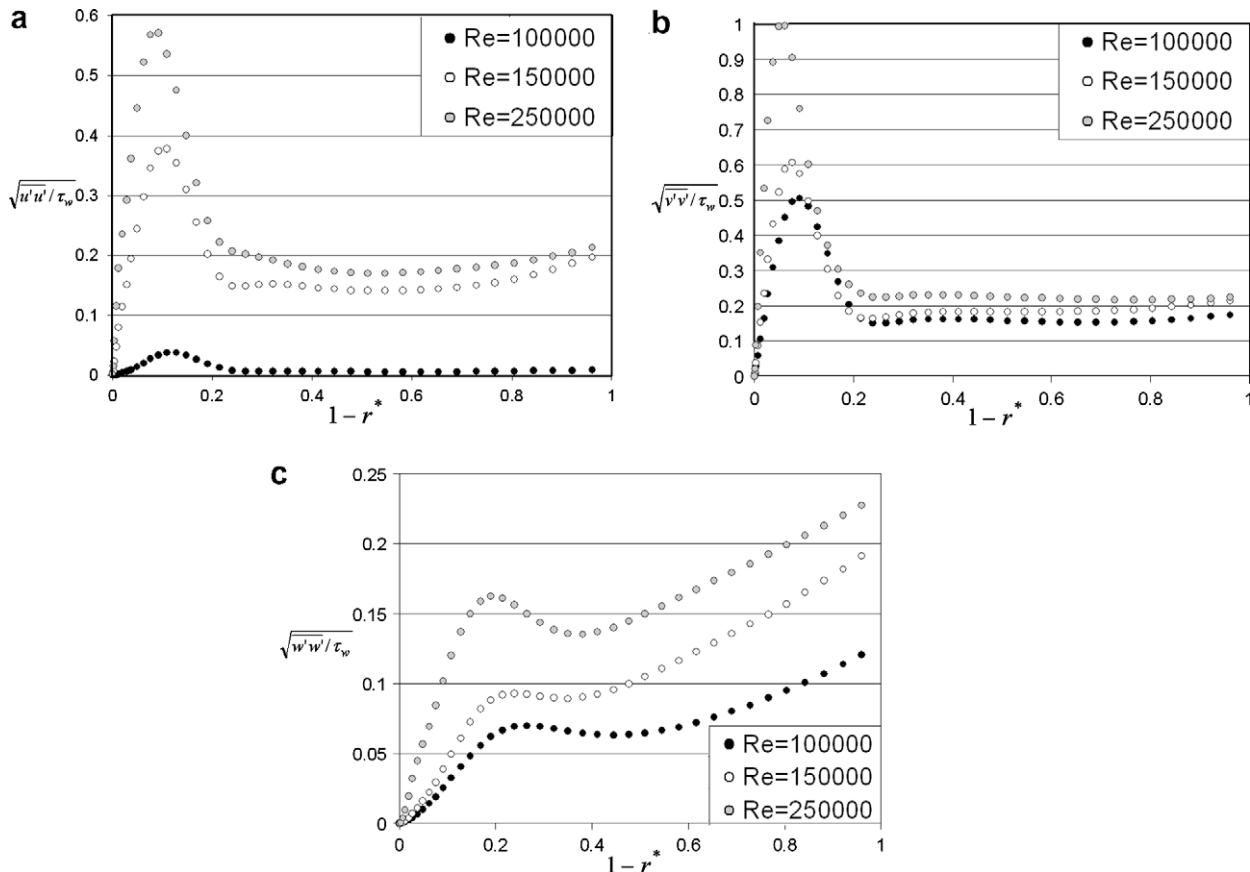

Fig. 15. The comparison between axial distributions of the normal Reynolds stress tensor components in the rotor boundary layer, normalized with the wall friction. (a) $\sqrt{\overline{u'u'}/\tau_w}$, (b) $\sqrt{\overline{v'v'}/\tau_w}$, and (c) $\sqrt{\overline{w'w'}/\tau_w}$, obtained in the middle section of cavity ($L = 5$, $Rm = 3$, $B = 0.1$) for different Reynolds numbers.
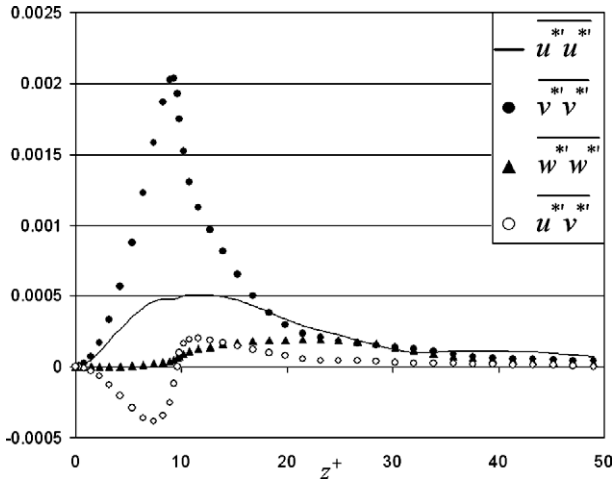
Fig. 16. The three main Reynolds stress tensor component profiles $\overline{u^{*\prime}u^{*\prime}}, \overline{v^{*\prime}v^{*\prime}}, \overline{w^{*\prime}w^{*\prime}}$ and one shear component $\overline{u^{*\prime}v^{*\prime}}$ in terms of z^+ obtained for ($L = 5$, Rm = 3, Re = 100,000, $B = 0.1$) in the middle section of the cavity.
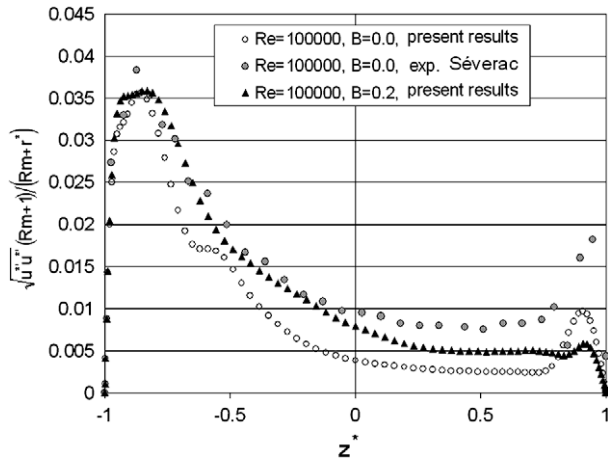
Fig. 17. Axial profiles of the radial Reynolds stress component $\sqrt{\overline{u^{\prime}u^{\prime}}}(\mathrm{Rm}+1)/(\mathrm{Rm}+r^*)$ in terms of z^* ($L = 5$, Rm = 1.8, Re = 100,000, $B = 0.0$, 0.2). Comparison with the experimental results of Séverac et al. (2007).
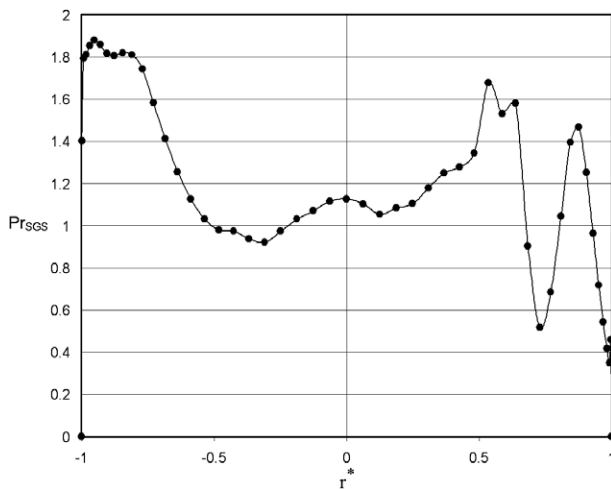
Fig. 18. Axial profile of the averaged in time and azimuthal direction Pr_{SGS} computed from Eq. (11) in function of z^* ($L = 9$, Rm = 1.5, Re = 150,000, $B = 0.1$, $r^* = 0$).

very similar to those obtained from Nikitenko (1963) correlation function:

$$\mathrm{Nu}_r = 0.675 \mathrm{Re}_r^{0.5} \tag{15b}$$

Fig. 20 shows the averaged Nusselt numbers Nu_{avg} in terms of Reynolds numbers obtained for the rotor boundary layer of the cavities with aspect ratios $L = 5$ and 9. Nu_{avg} is defined in the following manner:

$$\mathrm{Nu}_{avg} = \frac{\int_{R_0}^{R_1} \mathrm{Nu}_r(r)2\pi r \, \mathrm{d}r}{\pi \left(R_1^2 - R_0^2\right)} \tag{16}$$

We can see that the values of Nu_{avg} increase almost linearly with increasing Re. The present rotor boundary layer results are correlated by the following law:

$$\mathrm{Nu}_{avg} = 0.0087 \mathrm{Re}^{0.7911} \tag{17}$$

In Fig. 20 the present averaged Nusselt numbers are compared with the results obtained from correlation formulas proposed by Daily and Nece (1960) for regime II and IV:

$$\mathrm{Nu}_{avg,II} = \frac{2}{\pi} \left(\frac{1}{2L}\right)^{0.1} \mathrm{Re}^{0.5} \tag{18a}$$
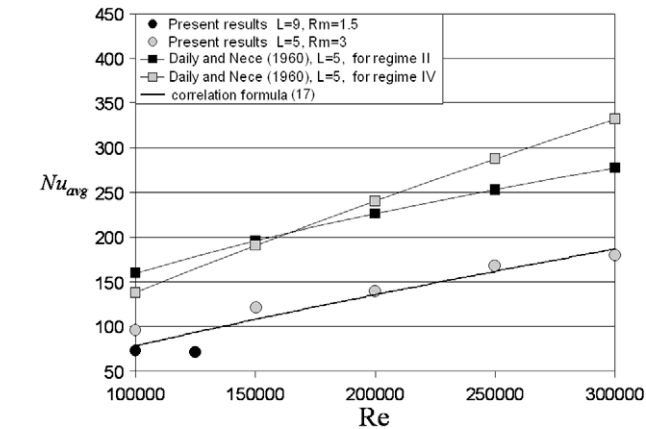
$$\mathrm{Nu}_{avg,IV} = \frac{0.545}{\pi} \left(\frac{1}{2L}\right)^{0.1} \mathrm{Re}^{0.8} \tag{18b}$$
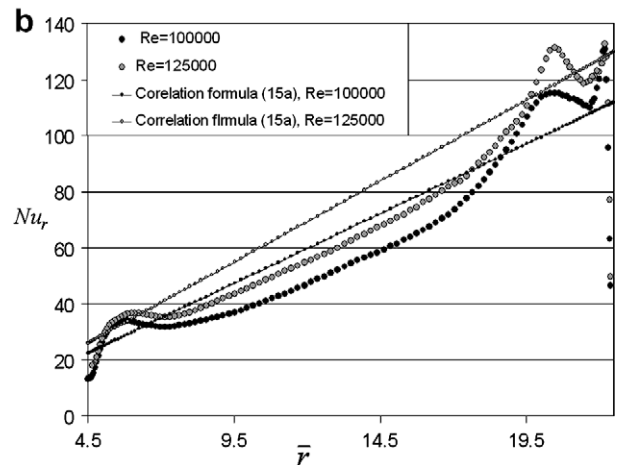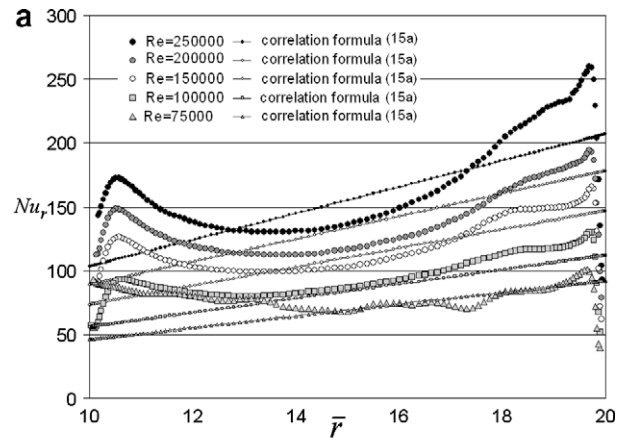
Fig. 19. Distributions of the local Nusselt numbers in terms of dimensionless radius $\bar{r}$ along the rotor for different Reynolds numbers for the cavities. (a) ($L = 5$, Rm = 3, $B = 0.1$) and (b) ($L = 9$, Rm = 1.5, $B = 0.1$). Comparison with the results obtained from the correlation formulas.
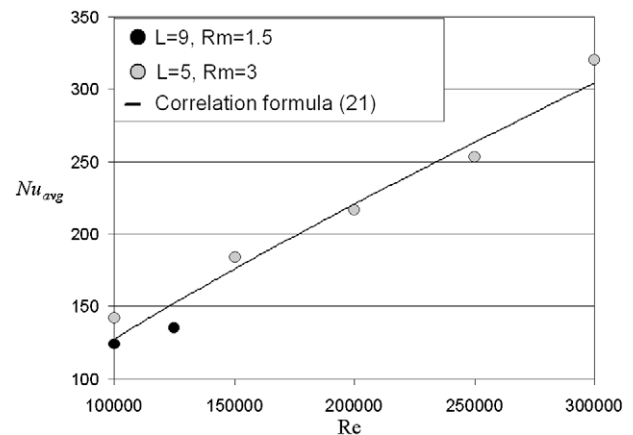
5.2. Distribution of the local Nusselt numbers on the stator

Fig. 21a and b show distributions of the local Nusselt number Nu_r on the stator, in terms of dimensionless radius $\bar{r}$, obtained for cavities ($L = 5$, Rm = 3, $B = 0.1$) and ($L = 9$, Rm = 1.5, $B = 0.1$),

respectively. We can see that for the cavity with aspect ratio $L = 5$ the linear dependence between Nu_r and radius $\bar{r}$ holds for $\bar{r} < \sim 18$. Then the curves change their slopes and exhibit an enhancement in the heat transfer. We observe a significant increase of Nu_r with the increasing Reynolds number. Based on these results, we propose a correlation function:

Fig. 20. The averaged Nusselt numbers Nu_{avg} in terms of Reynolds numbers obtained for the rotor boundary layer of the cavities ($L = 5$, Rm = 3, $B = 0.1$) and ($L = 9$, Rm = 1.5, $B = 0.1$). Comparison with the results obtained from correlation formulas proposed by Daily and Nece (1960) for regime II and IV.
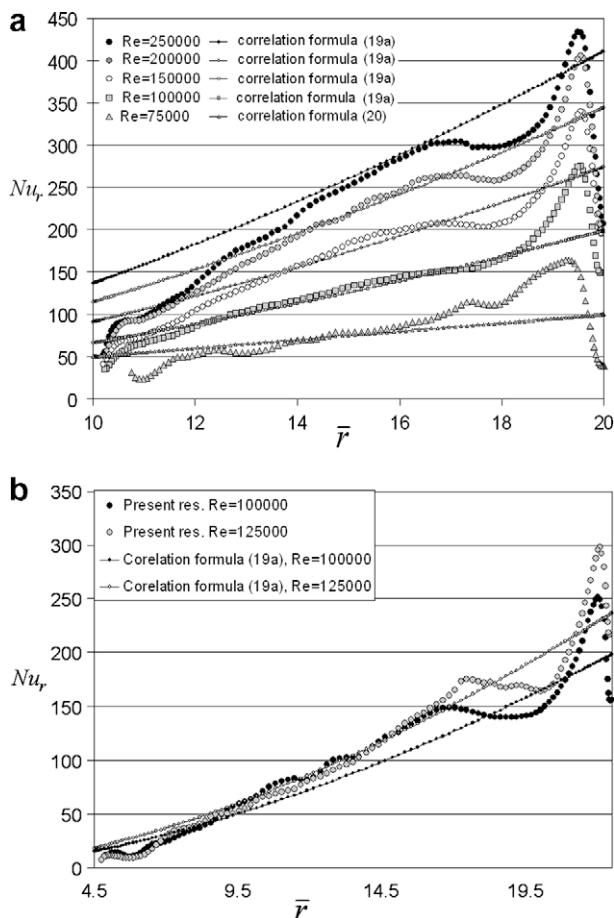

Fig. 22. The averaged Nusselt numbers Nu_{avg} in terms of Reynolds numbers obtained for the stator boundary layer of the cavities ($L = 5$, Rm = 3, $B = 0.1$) and ($L = 9$, Rm = 1.5, $B = 0.1$).

Fig. 21. Distributions of the local Nusselt numbers in terms of dimensionless radius $\bar{r}$ along the stator for different Reynolds numbers for the cavities. (a) ($L = 5$, Rm = 3, $B = 0.1$) and (b) ($L = 9$, Rm = 1.5, $B = 0.1$). Comparison with the results obtained from the correlation formulas.
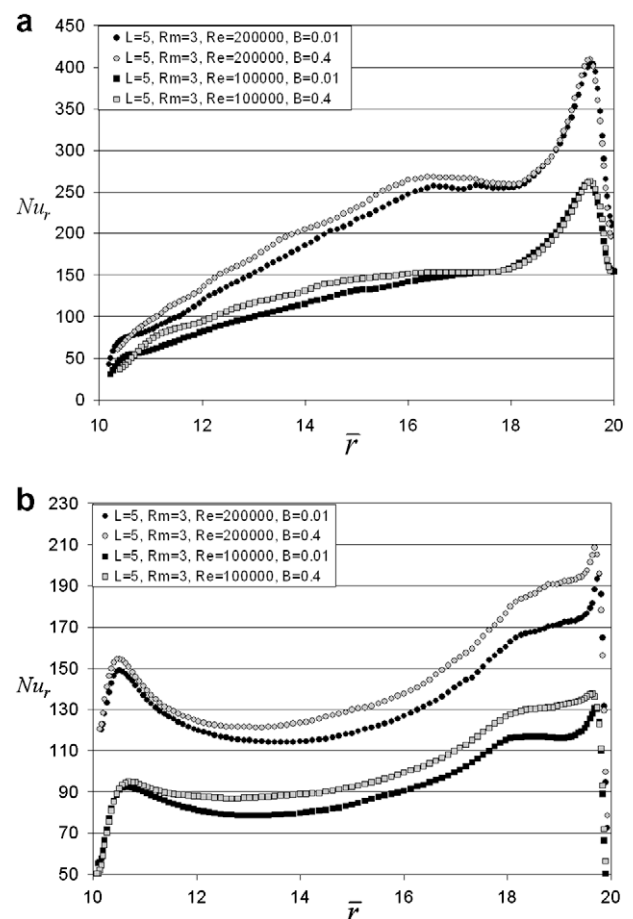
Fig. 23. Distributions of the local Nusselt numbers in terms of dimensionless radius $\bar{r}$ along (a) the stator, (b) rotor, obtained for $B = 0.01$ and $B = 0.4$ ($L = 5$, Rm = 3, Re = 100,000 and 200,000).

$$Nu_r = 0.021Re_r^{0.795} \tag{19a}$$

This correlation formula is very close to the formula proposed by Nikitenko (1963) for turbulent flow:

$$Nu_r = 0.0178Re_r^{0.8} \tag{19b}$$

The lines obtained from correlation function (19a) for Re = 100,000–250,000 are included in Fig. 21a. Distribution obtained by the LES for Re = 75,000 is compared with the result obtained from Nikitenko (1963) formula for the laminar stator boundary layer.

$$Nu_r = 0.364Re_r^{0.5} \tag{20}$$

Fig. 22 shows the averaged Nu_{avg} values in terms of the Reynolds number, obtained for the stator. We correlate our results by the following law:

$$Nu_{avg} = 0.0142Re^{0.7909} \tag{21}$$

5.3. Influence of the thermal Rossby number

To analyze the influence of the thermal Rossby number on local Nusselt number distributions along disks, we have performed the computations for the thermal Rossby number from the range $B = 0.01$–0.4. In the present research we have found that the influence of the thermal Rossby number on the basic state (Fig. 5) as well as on the distribution of the local Nusselt numbers is not large. Exemplary distributions of Nu_r along the stator and rotor, obtained for $B = 0.01$ and $B = 0.4$ ($L = 5$, Rm = 3, Re = 100,000 and 200,000) are presented in Fig. 23a and b, respectively. We can see that the largest increase takes place in the middle part of stator; the maximum increment equals about 25. The maximum increment along the rotor is observed near the outer cylinder with maximum value about 20. The same order of increase in the local Nusselt number is observed for cavity ($L = 9$, Rm = 1.5, Re = 100,000 and 125,000).

The influence of the thermal Rossby number on the distribution of the averaged Nusselt numbers in terms of Re is negligible.

6. Conclusions

In this paper we presented Large Eddy Simulation of the non-isothermal transitional and turbulent flows in sealed cavities with aspect ratio $L = 5$ and 9. In the LES we used a version of the dynamic Smagorinsky eddy viscosity model proposed by Meneveau (1996), in which the Smagorinsky coefficients are averaged along fluid pathlines. This algorithm turned out to be very effective and allowed us to perform computations for higher Reynolds numbers.

Computations have been performed for the thermal Rossby number from the range $B = 0.01$–0.4 (with heated stator and outer cylinder) and for Reynolds numbers up to Re = 300,000 for the cavity with the aspect ratio $L = 5$, and for Reynolds number up to Re = 150,000 for the cavity with $L = 9$. The investigated flows belong to the Batchelor family (the flows are divided into two boundary layers separated by a central rotating inviscid core). In the considered range of parameters the rotor boundary layer is laminar, whereas the stator boundary layer is turbulent. We have found that the intensity of the fluid turbulence in the stator boundary layer increases towards the outer cylinder. In the rotor boundary layer we observed 3D spiral vortices recognized as the type I instability. In the fully turbulent stator boundary layer ($L = 5$, Rm = 3) the structures are thinner and aligned in the azimuthal direction. The polar profiles fall between the laminar solution and the typical turbulent profiles presented in the paper by Lygren and Andersson (2001). The LES results have been compared with the DNS result

obtained for a more refined mesh. To verify our results the obtained axial distribution of the radial Reynolds stress tensor component in the middle section of cavity were compared with the experimental results of Séverac et al. (2007). Comparison shows a good agreement.

We analyzed the distributions of the local Nusselt numbers along the stator and the rotor obtained for different Reynolds numbers and different thermal Rossby numbers. The computations have shown that the Nusselt number distributions reflect the flow structure. We observed a rapid enhancement in the heat transfer in the outer end-wall area where the intensity of turbulence is the largest. We have found that the heat transfer depends strongly on the Reynolds number and that the influence of the thermal Rossby number on the local Nusselt number distributions in the considered range of B is small. We proposed correlation formulas for predicting distributions of the local Nusselt numbers along the rotor and stator. The averaged Nusselt numbers in terms of the Reynolds numbers were analyzed and the proposed correlation formulas were compared with those published by Daily and Nece (1960) for regime II and IV.

References

Abe, K., Kondoh, T., Nagano, Y., 1996. A two-equations heat transfer model reflecting second moment closures for wall and free turbulence flows. Int. J. Heat Fluid Flow 17, 228–237.

Andersson, H.I., Lygren, M., 2006. LES of open rotor–stator flow. Int. J. Heat Fluid Flow 27 (4), 551–557.

Chew, J.W., Vaughan, C.M., 1988. Numerical predictions for the flow induced by an enclosed rotating disc. In: 33rd Gas Turbine Conf., Amsterdam, ASME Paper 88-GT-127.

Cobb, E.C., Saunders, O.A., 1956. Heat transfer from a rotating disk. Proc. Roy. Soc. A 236, 343–351.

Craspo del Arco, E., Maubert, P., Randriamampianina, A., Bontoux, P., 1996. Spatio-temporal behavior in a rotating annulus with a source sink flow. J. Fluid Mech. 328, 271–296.

Czarny, O., Iacovides, H., Launder, B.E., 2002. Processing vortex structure in turbulent flow within rotor–stator disc cavities. Turbul. Combust. 69 (1), 51–61.

Daily, J.W., Nece, R.E., 1960. Chamber dimension effects on induced flow and frictional resistance of enclosed rotating disks. J. Basic Eng. 82, 217–232.

Djaoui, M., Debuchy, R., 1998. Heat transfer in a rotor-stator system with a radial inflow. C.R. Acad. Sci. Paris II B 326, 309–314.

Dorfman, L.A., 1963. Hydrodynamic Resistance and Heat Loss from Rotating Solids. Oliver and Boyd, Edinburgh and London.

Elena, L., Schiestel, R., 1995. Turbulence modeling of confined flow in rotating disk systems. AIAA J. 33 (5), 812–821.

Elena, L., Schiestel, R., 1996. Turbulence modeling of rotating confined flows. Int. J. Heat Fluid Flow 17, 283–289.

Germano, M., Piomelli, U., Moin, P., Cabot, W., 1991. A dynamic sub-grid eddy viscosity model. Phys. Fluids A 3 (7), 1760–1765.

Goldstein, S., 1935. On the resistance to the rotation of a disc immersed in a fluid. Proc. Camb. Philos. Soc. 31, 232–241.

Healey, J.J., 2007. Enhancing the absolute instability of a boundary layer by adding a far-away plate. J. Fluid Mech. 579, 29–61.

Hugues, S., Randriamampianina, A., 1998. An improved projection scheme applied to pseudospectral methods for the incompressible Navier–Stokes equations. Int. J. Numer. Methods Fluids 28, 501.

Iacovides, H., Toumpanakis, P., 1993. Turbulence modelling of flow in axisymmetric rotor–stator systems. In: Proceedings of Fifth International Symposium on Refined Flow Modelling and Turbulence Measurements, Paris.

Itoh, M., Yamada, Y., Imao, S., Gonda, M., 1990. Experiments on turbulent flow due to an enclosed rotating disk. In: Ganic, E., Rodi, W. (Eds.), Engineering Turbulence Modeling and Experiments. Elsevier, New York, pp. 659–668.

Jacques, R., Le Quéré, P., Daube, O., 2002. Axisymmetric numerical simulations of turbulent flow in a rotor stator enclosures. Int. J. Heat Fluid Flow 23, 381–397.

Launder, B.E., Sharma, B., 1974. Application of the energy dissipation model of turbulence to the calculation of the flow near a spinning disk. Lett. Heat Mass Transfer 1 (2), 131–138.

Lilly, D., 1992. A proposed modification of the Germano subgrid-scale closure method. Phys. Fluids A 4 (3), 633–635.

Lopez, J., Hart, J., Marques, F., Kittelman, S., Shen, J., 2002. Instability and mode interactions in a differentially driven rotating cylinder. J. Fluid Mech. 462, 383–409.

Lygren, M., Andersson, H.I., 2001. Turbulent flow between a rotating and a stationary disk. J. Fluid Mech. 426, 297.

Lygren, M., Andersson, H.I., 2004. Large eddy simulations of the turbulent flow between a rotating and a stationary disk. ZAMP 55, 268.

Meneveau, C., Lund, T.S., Cabot, W.H., 1996. A Lagrangian dynamic subgrid-scale model of turbulence. J. Fluid Mech. 319, 353–385.

Moisy, F., Doaré, O., Pasutto, T., Daube, O., Rabaud, M., 2004. Experimental and numerical study of the shear layer instability between two counter-rotating disks. J. Fluid Mech. 507, 175–202.

Morse, A., 1987. Numerical prediction of turbulent flow in rotating cavities. In: Gas Turbine Conf. and Exhibition, Anaheim, CA, ASME Paper 87-GT-74.

Nagano, Y., Tagawa, M., Tsuji, T., 1991, An improved two-equation heat transfer model for wall turbulent shear flow. In: Proc. of the ASME/JSME Thermal Engineering Joint Conference, vol. 3, pp. 233–240.

Nikitenko, N.I., 1963. Experimental investigation of heat exchange of a disk and a screen. J. Eng. Phys. 6, 1–11.

Owen, J.M., Haynes, C.M., Bayley, F.J., 1974. Heat transfer from an air-cooled rotating disc. Proc. Roy. Soc. A 336, 453–473.

Owen, J.M., Rogers, R.H., 1989. Flow and heat transfer in rotating-disc systems. Volume I: Rotor stator systems. In: Morris, W.D. (Ed.). Wiley, Taunton, Somsert, England.

Owen, J.M., Rogers, R.H., 1995. Flow and heat transfer in rotating-disc systems. Volume I: Rotor stator system. In: Morris, W.D. (Ed.). Wiely, Taunton, Somsert, England.

Pasquetti, R., 2006. Spectral vanishing viscosity method for large eddy simulation of turbulent flow. J. Sci. Comp. 27 (1–3), 365–375.

Pellé, J., Harmand, S., 2007. Heat transfer measurements in an opened rotor–stator system air-gap. Exp. Therm. Fluid Sci. 31, 165–180.

Poncet, S., Schiestel, R., 2007. Numerical modeling of heat transfer and fluid flow in rotor–stator cavities with throughflow. Int. J. Heat Mass Transfer 50 (7–8), 1528–1544.

Poncet, S., Serre, E., 2008, Large eddy Simulation of non-isothermal turbulent rotor–stator flows. In: The 12th International Symposium on Transport Phenomena and Dynamics of Rotating Machinery, Honolulu, Hawaii, ISROMAC12-2008-2009.

Randriamampianina, A., Poncet, S., 2006. Turbulence characteristics of the Bödewadt layer in a large enclosed rotor–stator system. Phys. Fluids 18, 055104.

Randriamampianina, A., Elena, L., Fontaine, J.P., Schiestel, R., 1997. Numerical prediction of laminar, transitional and turbulent flows in shrouded rotor–stator systems. Phys. Fluids 9 (6), 1696–1713.

Randriamampianina, A., Bontoux, P., Roux, B., 1987. Ecoulements induits par la force gravifique dans une cavité cylindrique en rotation. Int. J. Heat Mass Transfer 30 (7), 1275–1292.

Randriamampianina, A., Schiestel, R., Wilson, M., 2001. Spatio-temporal behavior in an enclosed corotating disk pair. J. Fluid Mech. 434, 39.

Raspo, I., Hugues, S., Serre, E., Randriamampianina, A., Bontoux, P., 2002. A spectral projection methods for the simulation of complex three-dimensional rotating flows. Comput. Fluids 31 (4–7), 745–767.

Schukin, V.K., Olimpiev, V.V., 1975. Heat transfer of disc rotating in a housing with transitional and turbulent boundary layer. Soviet Aeronaut. 18, 77–81.

Serre, E., Pulicani, J.P., 2001. A three-dimensional pseudospectral method for rotating flows in a cylinder. Comput. Fluids 30, 491.

Serre, E., Crespo del Arco, E., Bontoux, P., 2001. Annular and spiral patters in flow between rotating and stationary disks. J. Fluid Mech. 434, 65–100.

Serre, E., Bontoux, P., Launder, B.E., 2004a. Transitional–turbulent flow with heat transfer in a closed rotor–stator cavity. J. Turbul. 5, 8.

Serre, E., Tuliszka-Sznitko, E., Bontoux, P., 2004b. Coupled numerical and theoretical study of the transition flow between a rotating and stationary disk. Phys. Fluids 16 (3), 688–707.

Séverac, E., Poncet, S., Serre, E., Chauve, M.P., 2007. Large eddy simulations and measurements of turbulent enclosed rotor–stator flows. Phys. Fluids 19, 085113-1–17.

Séverac, E., Serre, E., 2007. A spectral viscosity LES for the simulation of turbulent flows within rotating cavities. J. Comp. Phys. 226 (2), 1234–1255.

Tavener, S.J., Mullin, T., Cliffe, K.A., 1991. Novel bifurcation phenomena in a rotating annulus. J. Fluid Mech. 229, 483–497.

Tuliszka-Sznitko, E., Serre, E., Bontoux, P., 2002. On the nature of the boundary layers instabilities in a flow between a rotating and a stationary disc. C.R. Acad. Sci. Paris II B – Mech. 330 (2), 91–99.

Tuliszka-Sznitko, E., Zieliński, A., 2007. Instability of the flow in rotating cavity. J. Theor. Appl. Mech. 45, 685–704.

Tuliszka-Sznitko, E., Zielinski, A., 2008. DNS/LES of transitional flow in rotating cavity. Int. J. Transport Phenomena 10 (3), 223–234.

Tuliszka-Sznitko, E., Zielinski, A., Majchrowski, W., 2009. LES of turbulent and transitional flows in rotor/stator cavity. Archives of Mechanics, submitted for publication.

Wu, X., Squires, K.D., 2000. Prediction and investigation of the turbulent flow over a rotating disk. J. Fluid Mech. 418, 231–264.